H_2-reduced phosphomolybdate promotes room-temperature aerobic oxidation of methane to methanol

Sikai Wang [1,2], Victor Fung [3,4], Max J. Hülsey [2], Xiaocong Liang[5], Zhiyang Yu [5], Jinquan Chang[1,2], Andrea Folli[6], Richard J. Lewis [7], Graham J. Hutchings [7], Qian He [8] & Ning Yan [1,2,9]

The selective partial oxidation of methane to methanol using molecular oxygen (O_2) represents a long-standing challenge, inspiring extensive study for many decades. However, considerable challenges still prevent low-temperature methane activation via the aerobic route. Here we report a precipitated Pd-containing phosphomolybdate, which, after activation by molecular hydrogen (H_2), converts methane and O_2 almost exclusively to methanol at room temperature. The highest activity reaches 67.4 μmol g_{cat}^{-1} h^{-1}. Pd enables rapid H_2 activation and H spillover to phosphomolybdate for Mo reduction, while facile O_2 activation and subsequent methane activation occur on the reduced phosphomolybdate sites. Continuous production of methanol from methane was also achieved by concurrently introducing H_2, O_2 and methane into the system, where H_2 assists in maintaining a moderately reduced state of- pho-sp-ho-mo-ly-bdate-. This work reveals the underexplored potential of such a Mo-based catalyst for aerobic methane oxidation and highlights the importance of regulating the chemical valence state to construct methane active sites.

The selective oxidation of methane (CH_4) to organooxygen chemicals such as methanol (CH_3OH) using molecular oxygen (O_2) represents a long-standing challenge in chemistry[1–4]. However, despite decades of research, there is still no industrially viable direct route for methanol production from methane[5,6]. Indeed the large-scale production of methanol is reliant on the multistep (syngas) route, which operates at elevated temperatures and pressures[7]. In nature, the methane monooxygenase (MMO) class of enzymes represents a one-step aerobic route to methanol that operates under ambient conditions[8]. Many heterogeneous catalysts have also been developed for methane valorization using O_2 as the terminal oxidant[9–25], with relatively high temperatures typically applied (100–240 °C). Considerable attention has been placed on precious-metal-based catalysts; for instance, atomically dispersed rhodium (Rh) species have been shown to offer high efficacy when using carbon monoxide as a co-reductant[2]. By comparison, recent investigations have demonstrated the efficacy of supported gold (Au) nanoparticles in the absence of a co-reductant[10]. However, in both cases, considerable concentrations of over-oxidation products (such as acetic and formic acid) are also synthesized.

[1]Joint School of National University of Singapore and Tianjin University, International Campus of Tianjin University, Fuzhou, China. [2]Department of Chemical and Biomolecular Engineering, National University of Singapore, Singapore, Singapore. [3]Center for Nanophase Materials Sciences, Oak Ridge National Laboratory, Oak Ridge, TN, USA. [4]School of Computational Science and Engineering, Georgia Institute of Technology, Atlanta, GA, USA. [5]State Key Laboratory of Photocatalysis on Energy and Environment, College of Chemistry, Fuzhou University, Fuzhou, China. [6]Net Zero Innovation Institute, Cardiff Catalysis Institute, School of Chemistry, Cardiff University, Cardiff, UK. [7]Max Planck Centre on the Fundamentals of Heterogeneous Catalysis FUNCAT, Cardiff Catalysis Institute, School of Chemistry, Cardiff University, Cardiff, UK. [8]Department of Materials Science and Engineering, National University of Singapore, Singapore, Singapore. [9]Centre for Hydrogen Innovations, National University of Singapore, Singapore, Singapore. e-mail: Hutch@cardiff.ac.uk; heqian@nus.edu.sg; ning.yan@nus.edu.sg

Alternative approaches to methane oxidation, which operate at mild temperatures, have been investigated. In particular, significant focus has been placed on the utilization of hydrogen peroxide (H_2O_2) as the oxidant, which produces hydroxyl ($HO^•$) and hydroperoxyl ($HOO^•$) radicals[21,26,27] or interacts with surface metal sites to generate active oxygen-containing groups to achieve methane activation, with these latter materials able to compete with MMO on an activity basis[9,17]. How-ever, whilst methane valorization using commercially synthesized H_2O_2 may be promising on an academic scale, the economic and technical challenges associated with H_2O_2 formation via current industrial routes, as well as concerns associated with the safe transport and storage of the oxidant, are likely to preclude the use of H_2O_2 for methane upgrading on an industrial level[28]. Towards this end, important progress has been made recently by Jin et al. and other groups, who demonstrated the efficacy of H_2O_2 generated in situ for methanol synthesis[21,24,29–31]. Under light irradiation, $HO^•$ radicals formed in situ over photocatalysts also initiate effective methane conversion to methanol[32–34]. Despite these advancements, however, notable methane oxidation activities still rely on external energies such as heat and illumination.

To conceive fresh ideas for designing thermal catalysts for meth-ane oxidation, we once again draw inspiration from the MMO class of enzymes. During the enzymatic process, a reductase or other electron-donating cofactor partially reduces the iron or copper active sites with the MMO, which subsequently interact with O_2 to create active oxygen-containing species for selective methane oxidation[4,35]. We postulate that regulating the chemical valence state of metal sites, in particular to generate partially reduced metal centres, may be a promising strategy that enables the oxidation potential of O_2 to be harnessed under ambient conditions.

Polyoxometalates (POMs), such as phosphomolybdate (PMA; $[PMo_{12}O_{40}]^{3-}$), are a group of inorganic polyatomic ion clusters with numerous catalytic applications[36–39]. Keggin-structured PMA is a globe-like cluster comprised of a central phosphate caged by twelve interlinked MoO_6 units with molybdenum (Mo) in a high oxidation state. By immobilizing palladium (Pd) onto Mo-based POMs, we previously observed the facile reduction of Mo by hydrogen spillover from Pd at ambient temperature[40]. Here we demonstrate that the Pd-supported caesium-exchanged phosphomolybdate (Pd/CsPMA) catalyst offers considerable activity for the aerobic oxidation of methane to methanol at ambient temperature. Although the as-prepared Pd/CsPMA catalyst is inactive, after pretreatment in H_2 the reduced catalyst (Pd/CsPMA-H) converts methane and O_2 to methanol with ~100% selectivity and a productivity of 67.4 μmol g_{cat}^{-1} h^{-1}. The catalyst also produces methanol from methane in a mixed H_2/methane/O_2 atmosphere. In sharp contrast to previous studies where H_2O_2, $HO^•$ radicals and/or Pd sites are actively involved in the C–H activation of methane[22,29], our mechanistic studies strongly suggest that the activation of O_2 and methane for methanol occurs directly on the reduced PMA.

Results

Structural features and redox properties of Pd/CsPMA

The Pd/CsPMA catalyst was prepared by precipitating PMA anions ($[PMo_{12}O_{40}]^{3-}$) with Cs^+ and Pd^{2+} at subambient temperatures. The separated yellow solids, as observed via scanning electron microscopy and transmission electron microscopy, are spherical particles with a size ranging from approximately 50 to 300 nm (Supplementary Figs. 1 and 2). X-ray diffraction results suggest that the Pd/CsPMA material has a cubic crystal structure that is distinct from those of MoO_3 and PMA (Fig. 1a). From integrated differential phase contrast (iDPC) imag-ing, the crystals are assembled from individual PMA units (Fig. 1b and Supplementary Figs. 3–5), on the basis of which a structural model of the Pd/CsPMA material was constructed (Supplementary Fig. 6). Pd/ CsPMA and PMA gave similar Raman spectra, suggesting the preserva-tion of the anion structure during the catalyst synthesis (Fig. 1c). The actual Pd loading of Pd/CsPMA was determined to be 0.23 wt%, using inductively coupled plasma optical emission spectroscopy. The Pd species are distributed evenly on Pd/CsPMA, as shown in the high-angle annular dark-field (HAADF) imaging results under scanning transmis-sion electron microscopy (STEM) mode (Fig. 1d). X-ray photoelectron spectroscopy (XPS) analysis (Fig. 1e) and in situ diffuse reflectance infrared Fourier transform spectroscopy (DRIFTS) with nitric oxide (NO) as the probe molecule (Fig. 1f) confirm that Pd exists as charged Pd cations that are probably situated at the four-fold hollow sites of PMA by replacing Cs^+, as indicated in previous studies on single-atom POM systems[38,41].

When Pd/CsPMA was exposed to a flow of forming gas (5% H_2 in molecular nitrogen (N_2)) at room temperature (24 °C), a rapid colour change from yellow to dark blue was observed within twenty minutes. The in situ H_2-DRIFTS spectrum of Pd/CsPMA presents a notable peak at >3200 cm^{-1} for Pd/CsPMA (Supplementary Fig. 7), indicating the formation of a large amount of surface hydroxyl groups (–OH), which is not the case for CsPMA. This implies that Pd plays a crucial role in dissociating H_2 into hydrogen atoms and transferring hydrogen spe-cies from the noble metal sites to the support[42,43]. The hydrogen atoms donate electrons to PMA and combine with PMA oxygen atoms to form hydroxyl groups on the surface. In situ NO-DRIFTS analysis confirms that the Pd species remain highly dispersed during H_2 treatment at room temperature (Supplementary Fig. 8). We then prepared the Pd/ CsPMA-H material, by treating the unactivated Pd/CsPMA catalyst under H_2 (4 bar) in water for 15 min. As shown in Fig. 1g, the colour of the catalyst also changed from yellow (Pd/CsPMA) to dark blue (Pd/ CsPMA-H). Ultraviolet-visible (UV-visible) adsorption spectra of the Pd/CsPMA-H suspension showed a clear decrease in the Mo(VI) signal at 320–340 nm (Fig. 1h) and an increase in Mo(V) and Mo(IV) in the range of 600–900 nm (Fig. 1h inset), illustrating the reduction of Mo by hydrogen spillover[44,45]. As determined via redox titration using acidified $FeCl_3$ solution (Supplementary Fig. 9), each POM anion, on average, accepts 8.4 electrons after 15 min of H_2 treatment, corroborating the UV-visible adsorption data that Mo(VI) was only partially reduced. Addi-tional H_2 treatment does not increase the degree of hydrogen spillover.

The reduced Pd/CsPMA-H powder is readily re-oxidized when exposed to air at room temperature (represented as Pd/CsPMA-H-O), as judged from the recovered yellowish colour and the UV-visible absorp-tion results (Fig. 1g,h). This highlights that the reduced Pd/CsPMA catalyst can activate O_2 at ambient temperature. Pd/CsPMA-H-O exhibits a similar morphology and crystalline structure as well as characteristic POM anion Raman peaks to those of pristine Pd/CsPMA (Supplemen-tary Figs. 1 and 10 and Fig. 1a,c), which prove that the repeated reduc-tion–oxidation steps do not change the structure of Pd/CsPMA, thus hinting at its potential as a catalyst in redox reactions.

Catalytic performance in partial methane oxidation

The methane oxidation reaction was carried out at room temperature in an aqueous solution with methane and O_2 (ref. 46). The unactivated Pd/CsPMA catalyst exhibited negligible methane conversion activ-ity (Table 1, entry 1), and after the reaction the yellow colour of Pd/ CsPMA was maintained, indicating an unchanged oxidative state of Mo (Supplementary Fig. 11). To validate that adding electrons to the catalyst is conducive to the aerobic oxidation of methane, Pd/CsPMA was first treated with H_2 in the liquid phase at room temperature to form the reduced catalyst Pd/CsPMA-H. When Pd/CsPMA-H was used for methane oxidation with O_2 under identical conditions for 30 min, we observed the conversion of methane with methanol as the sole product (5.2 μmol g_{cat}^{-1} h^{-1}; Table 1, entry 2). Shortening the reaction to 5 min provided a proportionally increased methanol production rate (28.8 μmol g_{cat}^{-1} h^{-1}), suggesting that Pd/CsPMA-H is only active in the initial stage of the reaction (Table 1, entry 3). By adjusting the partial pressures of methane and O_2, it was possible to improve the metha-nol productivity, with this metric rising to 67.4 μmol g_{cat}^{-1} h^{-1} (Table 1, entry 4). The colour of the spent catalyst changed to greenish yellow,

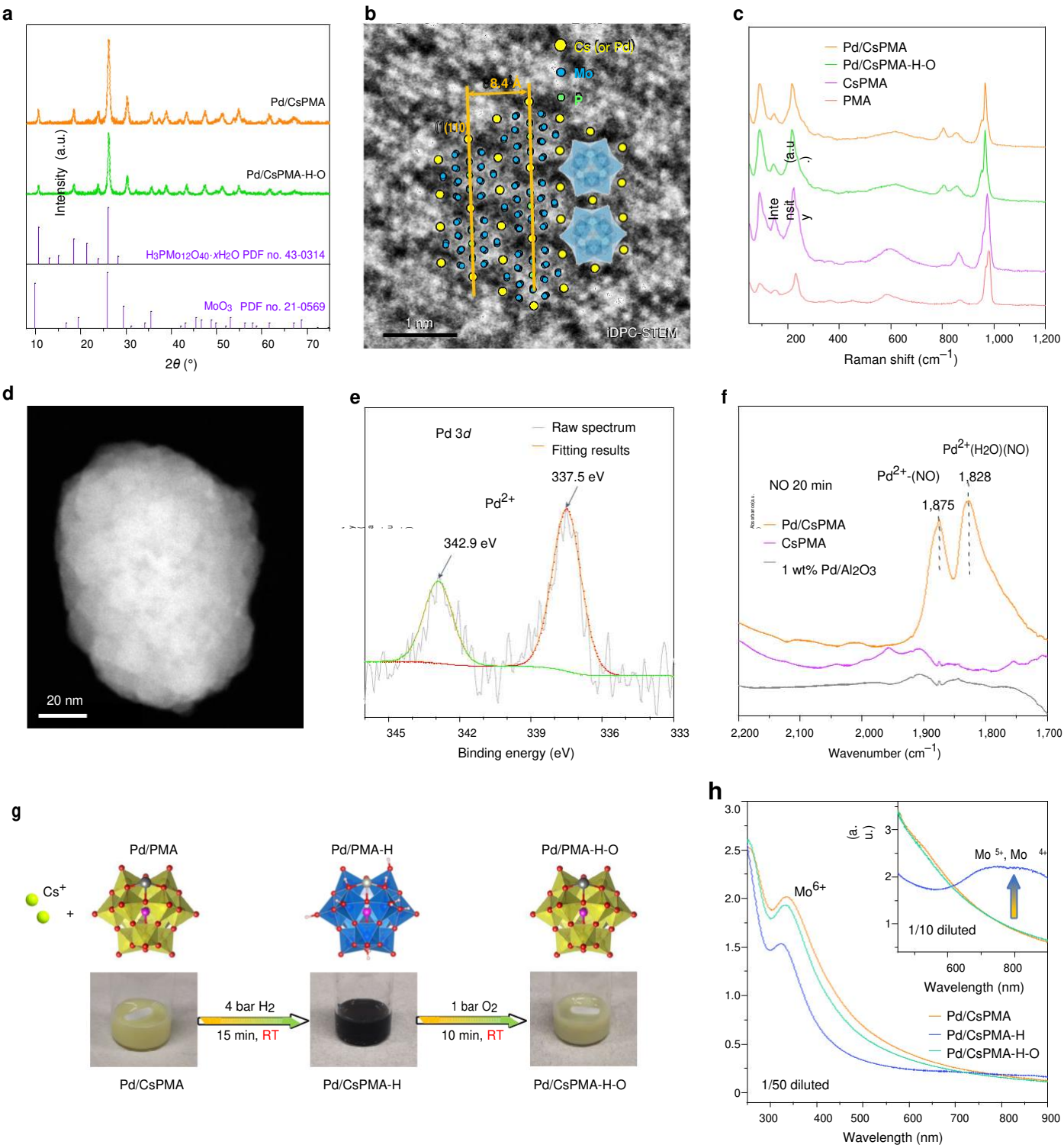

Fig. 1 | Structure and redox properties of Pd/CsPMA. a, X-ray diffraction spectra of Pd/CsPMA, Pd/CsPMA-H-O and the standard X-ray diffraction lines of $H_3PMo_{12}O_{40}$ (PMA) and MoO_3. PDF, powder diffraction file. **b**, Atomic resolution iDPC-STEM image of Pd/CsPMA. **c**, Raman spectra of PMA, CsPMA, Pd/CsPMA and Pd/CsPMA-H-O. **d**, HAADF-STEM image of Pd/CsPMA. **e**, Experimental and fitting results of the Pd 3*d* XPS spectrum of Pd/CsPMA. **f**, In situ NO-DRIFTS spectra of CsPMA, Pd/CsPMA and commercially available 1 wt% Pd/Al_2O_3. **g**, The reversible reduction/oxidation of Pd/CsPMA at room temperature (RT). **h**, UV-visible absorption spectra of suspensions of Pd/CsPMA, Pd/CsPMA-H and Pd/CsPMA-H-O. The catalyst suspensions (10 mg/2.0 ml water) were diluted with degassed water at a ratio of 1/50 and 1/10 (shown in the inset) for the measurement.

suggesting that it was re-oxidized by O_2 during the course of the reaction (Supplementary Fig. 11). These results highlight two important findings. First, the H_2-reduced Pd/CsPMA catalyst selectively transforms meth-ane and O_2 into methanol at room temperature. Second, Pd/CsPMA-H does not maintain its reduced state under an oxidizing atmosphere, and thus quickly loses its initial activity. To quantitatively establish the relationship between the degree of reduction of Pd/CsPMA and the methane oxidation activity, we performed H_2 treatments with varying

Table 1 | Oxidation of methane to methanol using the Pd/CsPMA catalyst

Entry	Conditions (numbers in parentheses denote the gas pressure (bar))	Methanol production ($\mu mol\ g_{cat}^{-1}\ h^{-1}$)	Methanol selectivity (%)	Specific activity ($mmol\ g_{Pd}^{-1}\ h^{-1}$)	Colour after reaction
1	Single step: CH_4(10) + O_2(1), 30 min	0	N/A	0	Yellow
2	Step 1: H_2(4). Step 2: CH_4(10) + O_2(1), 30 min	5.2	100.0	2.3	Yellow
3	Step 1: H_2(4). Step 2: CH_4(10) + O_2(1), 5 min	28.8	100.0	12.5	Green
4	Step 1: H_2(4). Step 2: CH_4(20) + O_2(0.3), 5 min	67.4	100.0	29.3	Green
5	Single step: CH_4(10) + H_2(4) + O_2(0.3), 30 min	28.5	100.0	12.4	Dark blue
6	Step 1: H_2(1). Step 2: CH_4(20) + H_2(1) + O_2(0.4), 8 h	18.1	74.0	7.9	Dark blue
7	Single step: CH_4(10) + H_2O_2, 30 min	0	N/A	0	Yellow
8	Step 1: H_2(4). Step 2: ascorbic acid, CH_4(10) + O_2(1), 5 min	42.2	100.0	18.4	Green
9	Step 1: H_2(4). Step 2: Na_2S, CH_4(10) + O_2(1), 5 min	48.0	100.0	20.9	Blue

Reaction conditions: D_2O (2.0 ml), catalyst (10 mg), 800 r.p.m., room temperature. For entry 1, CH_4 (10 bar), O_2 (1 bar) and N_2 (9 bar) were applied. For entries 2, 3, 8 and 9, the catalyst was treated with H_2 (4 bar) for 15 min at room temperature before running the reaction under the same conditions. For entry 6, the catalyst was pretreated with H_2 (1 bar) for 18 min instead. For entry 4, CH_4 (20 bar) was used. For entry 5, CH_4 (10 bar), H_2 (4 bar) and O_2 (0.3 bar) balanced with N_2 (25.7 bar) were applied. For entry 7, the solvent used was H_2O instead of D_2O, with the addition of H_2O_2 (400 μmol). For entries 8 and 9, ascorbic acid (1 μmol) and Na_2S (1 μmol) were added, respectively, after H_2 pretreatment but before charging with CH_4 and O_2.

durations and H_2 pressures to produce reduced Pd/CsPMA samples with different degrees of reduction. These samples were then used for methane oxidation tests (CH_4 (10 bar), O_2 (0.3 bar), N_2 (2.7 bar), 15 min reaction). The performance data indicate that a minimum reduction of five electrons per PMA molecule is necessary for Pd/CsPMA to be active (Supplementary Fig. 12). Concurrently, we observed a sigmoid-like relationship between the accumulated methanol productivity and the initial degree of reduction, with a prominent increase in methanol yield for PMA samples pre-reduced with five or six electrons. Although each PMA molecule can be reduced by approximately nine electrons using H_2, further reduction with an electron number greater than seven does not lead to an increase in the methanol yield.

Despite the encouraging outcomes, the oxidative atmosphere results in the rapid deactivation of active sites, which leads to a low ratio between the methanol produced (0.02 μmol) and the exposed PMA (0.55 μmol), of roughly 4%. To sustain a reduced catalyst state, we then carried out the methane oxidation reaction using a non-explosive gas mixture of H_2, O_2, methane and N_2 so that H_2 pretreatment was no longer applied. Under an optimized H_2/O_2 ratio, Pd/CsPMA presents a methanol productivity of 28.5 $\mu mol\ g_{cat}^{-1}\ h^{-1}$ (corresponding to a noble metal specific productivity of 12.4 $mmol\ g_{Pd}^{-1}\ h^{-1}$), again with methanol as the only liquid product detected together with negligible gas-phase product in a 30 min reaction (Table 1, entry 5). The activity and selectiv-ity compare favourably with most reported noble-metal-containing catalysts for the thermal aerobic oxidation of methane to methanol at room temperature (Supplementary Table 1). Interestingly, we observed that, in a typical 30 min reaction, the reaction proceeds at a higher rate during the second 15 min compared with the first, probably due to an induction period required to form the reduced catalyst that is active for methane oxidation (Supplementary Fig. 13). The H_2/CH_4 ratio remained almost constant during the reaction, suggesting that H_2 is not preferentially consumed by O_2 compared with methane (Supplementary Table 2).

The production of methanol did not show any further increase when the reaction time was extended from 30 to 60 min, probably due to the over-reduction of the catalyst (>7.5–8 electrons per PMA; Sup-plementary Fig. 13). To maintain the catalyst activity for a longer dura-tion, Pd/CsPMA was first partially reduced with H_2 and then exposed to a mixture of methane, H_2 and O_2, with the H_2/O_2 ratio adjusted to stabilize the PMA at around a six-electron reduced state (Supplementary Fig. 14). To our delight, methane was oxidized continuously to organic oxygenates for 8 h, resulting in a total methanol yield of 1.45 μmol and formic acid as the secondary product (Table 1, entry 6).

Xiao and colleagues previously reported[29] the selective oxidation of methane with H_2 and O_2 using AuPd alloy nanoparticles confined in a zeolite support. In that case, H_2O_2 was produced locally, which then acted as the oxidant for methane oxidation. By contrast, H_2O_2 is unlikely to be the key oxidant in our system since no H_2O_2 was detected when supplying a mixture of H_2 and O_2 over the catalyst (detection limit, 0.5 ppm; Supplementary Fig. 15). In addition, when external H_2O_2 was added, no methanol was detected after 30 min despite 54% of the H_2O_2 being decomposed (Table 1, entry 7, and Supplementary Table 3). Methanol was produced only when H_2O_2 was used together with H_2 (Supplementary Table 3), although the best activity (that is, 14.4 $\mu mol\ g_{cat}^{-1}\ h^{-1}$) was still not as high as the case when H_2 and O_2 are supplied. Molecular oxygen works better as an oxidant than H_2O_2 in our case, possibly because, as a weaker oxidant, O_2 enables the catalyst to maintain the desired reduced state under H_2.

Methane oxidation was carried out under various partial pressures (P) of methane, H_2 and O_2. The reaction is first order with respect to methane in the range of 0–15 bar (Fig. 2a), indicating that methane acti-vation participates in the rate-determining step. By contrast, the metha-nol yield as a function of the H_2/O_2 ratio follows a volcano-type curve, with the optimal pressure of H_2 being 4 bar and that of O_2 at 0.3 bar (Fig. 2b). A threshold H_2 partial pressure of 2 bar must be reached to create a state with a sufficient degree of Mo reduction for C–H bond activation. When O_2 was eliminated from the reaction system, only a trace amount of methanol was detected (2.0 $\mu mol\ g_{cat}^{-1}\ h^{-1}$), probably due to the residual O_2 in water.

Several control catalyst samples were studied to confirm the criti-cal role of reduced Mo species as catalytically active sites. CsPMA, Rh/CsPMA and Pt/CsPMA, which showed no reduction of PMA by H_2 at room temperature, exhibited no methanol productivity (Fig. 2c). Rh/CsPMA and Pt/CsPMA were then pretreated with H_2 at elevated temperature (50 °C and 100 °C, respectively). After the pretreatment, both catalysts turned dark blue, signalling Mo reduction, and in the following step both catalysts produced methanol from methane and O_2 at room temperature (Supplementary Table 4). When PMA was

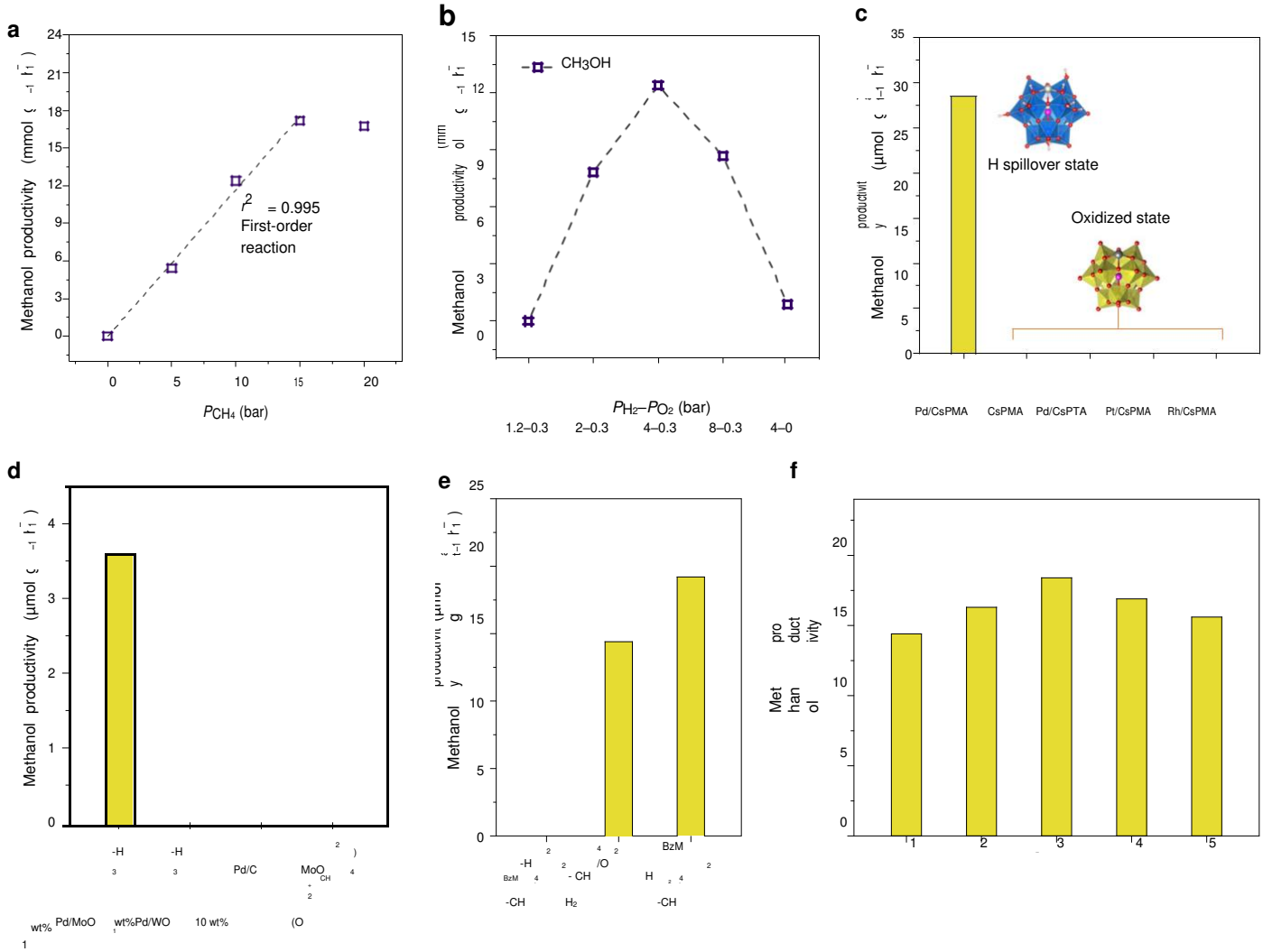

Fig. 2 | Parameter–activity correlations and recycling tests for methane oxidation. Reaction conditions (unless otherwise specified): catalyst (10 mg) in D_2O (2.0 ml), H_2 (4 bar), O_2 (0.3 bar), CH_4 (10 bar) balanced with N_2 (25.7 bar), room temperature, 30 min. **a**, Methanol productivity under various methane partial pressures using Pd/CsPMA. r^2, coefficient of determination. **b**, Methanol productivity under various partial pressures of H_2 and O_2. **c**, Methanol productivity for different POM-based catalysts. The loading of noble metals on the supported catalysts is around 0.25 wt%. The insets label the states of the catalysts during the reaction. Only Pd/CsPMA presents hydrogen spillover with H_2 (shown by a blue cluster), while the others stay in an oxidized state (shown by a yellow cluster). **d**, Methanol productivity using several traditional catalysts. For 1 wt% Pd/MoO_3-H and 1 wt% Pd/WO_3-H, the impregnated samples are treated with 5% H_2/N_2 forming gas at 300 °C. For MoO_2, O_2 (1 bar), CH_4 (10 bar) and N_2 (9 bar) were supplied without the addition of H_2. **e**, Poisoning tests using BzM to block the Pd sites (the reaction conditions are the same as annotated in Table 1, entry 3). BzM dissolved in ethanol was added into the reaction mixture before (left bar) or after (right bar) H_2 treatment (BzM:Pd = 2:1). For the control experiment without BzM (middle bar), the same amount of ethanol solvent was added after H_2 pretreatment before methane conversion. **f**, Recyclability testing of Pd/CsPMA for methane oxidation with O_2 and H_2 (reaction conditions: H_2 (2 bar), O_2 (0.3 bar), CH_4 (10 bar), 30 min).

replaced with phosphotungstate (PTA), Pd/CsPTA also did not show any methane activation under the same conditions (Fig. 2c and Supplemen-tary Fig. 7). Furthermore, Rb^+ and NH_4^+ were also used to precipitate PMA alongside Cs^+, giving Pd/RbPMA and Pd/NPMA, respectively. The as-formed Pd/RbPMA and Pd/NPMA, after H_2 reduction, presented similar methanol productivity values to Pd/CsPMA. This suggests that the cations in the catalysts do not largely affect the methane activation performance (Supplementary Fig. 16). To explore whether or not our finding, that is, H_2-reduced Mo in Pd/CsPMA readily converts methane and O_2 to methanol, is generalizable, 1 wt% Pd/MoO_3, 1 wt% Pd/WO_3 and 10 wt% Pd/C were evaluated under our methane oxidation conditions (Fig. 2d and Supplementary Table 5). The H_2-pretreated 1 wt% Pd/ MoO_3-H indeed exhibited a methanol productivity of 14.4 μmol g_{cat}^{-1} h^{-1} for a 5 min reaction, whereas the other two catalysts were inactive. Interestingly, MoO_2, with Mo(IV) as the only Mo species, showed no methane activation properties with O_2. The above results indicate that Pd can be substituted by other metals such as Pt or Rh to facilitate PMA reduction with H_2, and partially reduced Mo species are critical for methane activation with O_2.

Methanol formation pathway on reduced PMA: experimental evidence

Since the radical mechanism is one of the mainstream mechanisms to activate the methane C–H bond in aqueous solution, electron paramagnetic resonance (EPR) experiments using 5,5-dimethyl-1-pyrroline *N*-oxide radical trapping agent were carried out to determine the presence of reactive oxygen species (Supplementary Fig. 17)[47]. The appearance of characteristic quadruple peaks (1:2:2:1) for an H_2O_2 aqueous solution indicates trapped $HO^{\bullet}$ radicals, and triplet peaks was observed for an aqueous suspension of pristine Pd/CsPMA, probably coming from the

oxidative dimerization of 5,5-dimethyl-1-pyrroline N-oxide (ref. 48). However, these are the cases for which no methanol productivity was observed. By contrast, for the H_2-pretreated Pd/CsPMA-H catalyst, no simi-lar signals were detected. To provide further evidence that HO$^{\bullet}$ radicals do not operate in our system, methane oxidation reactions were carried out over the Pd/CsPMA-H catalyst in the presence of HO$^{\bullet}$ radical scavengers (that is, ascorbic acid or Na_2S) (Table 1, entries 8 and 9, respectively). For the reactions that included either ascorbic acid or Na_2S, the methanol productivity of the Pd/CsPMA-H catalyst did not decrease but instead increased to 42.2 and 48.0 μmol g_{cat}^{-1} h^{-1}, respectively, compared with 28.8 μmol g_{cat}^{-1} h^{-1} without the scavengers. This suggests that methane is not activated by free HO$^{\bullet}$ intermediates. The increased productivity may be ascribed to the elongated lifetime for reduced PMA species under O_2, due to the reductive nature of the scavengers.

To further rule out the role of Pd in C–H activation, selective poi-soning tests were conducted by adding benzyl mercaptan (BzM). BzM binds strongly with Pd, thus preventing Pd–reactant interactions (Fig. 3a and Supplementary Fig. 18)[40]. As expected, after introducing two equivalents of BzM (relative to Pd) to block Pd in Pd/CsPMA before H_2 treatment, PMA was unable to be reduced to enable methane oxida-tion ($BzM-H_2-CH_4/O_2$ in Fig. 2e). By contrast, when the same amount of BzM was added to pre-reduced Pd/CsPMA-H catalyst (H_2-BzM-CH_4/ O_2 in Fig. 2e), the methanol productivity mimicked the performance without BzM (H_2-CH_4/O_2 in Fig. 2e). This experiment, together with the earlier presented fact that reduced Rh/CsPMA and Pt/CsPMA are also active in the oxidation of methane to methanol at room temperature, provide compelling evidence that methane activation proceeds not on Pd sites but on reduced PMA.

The reduced catalyst Pd/CsPMA-H has considerable solubility in water, probably due to the strong interaction between spilt H-induced surface hydroxyl groups and water molecules[49,50]. This provides an opportunity to determine whether methanol formation requires an extended surface or individual PMA anions. Hence, a H_2-reduced Pd/CsPMA-H aqueous suspension was separated via ultrafiltration cen-trifugation (nominal molecular weight limit, 10 kDa) and evaluated in methane oxidation. The resulting solution and solid residue were both found to offer activity (Supplementary Fig. 19), suggesting that H_2-reduced PMA provides the active sites for methane conversion, regardless of whether in solution or the solid phase.

To enable catalyst recycling, the spent reaction solution was first re-oxidized using O_2 (1 bar) at room temperature, followed by the addi-tion of the Cs^+ salt as a precipitation agent. Over 99% of the Pd/CsPMA catalyst can be regenerated (Supplementary Table 6). A reductive atmosphere (H_2 (2 bar), O_2 (0.3 bar) and CH_4 (10 bar) diluted with N_2 to a total pressure of 40 bar) was used for the reaction sessions during successive recycling tests to ensure the sufficient activation of Mo in each cycle. No loss in methanol formation activity was observed over five successive reactions (Fig. 2f); furthermore, the recovered catalyst (after five cycles) exhibited an identical X-ray diffraction pattern to the fresh catalyst (Supplementary Fig. 20), indicating that the PMA structure remained intact during recycling.

In view of the important role of reduced PMA on methane activa-tion, we investigated the coordination structure around Mo before and after hydrogen reduction via pseudo in situ EPR. As expected, no signal was detected for Pd/CsPMA before H_2 treatment since the Mo species exist predominantly as Mo(VI), which is EPR-inactive (Sup-plementary Fig. 21)[51]. When measured under a H_2 atmosphere, Pd/ CsPMA-H exhibits a broad, featureless EPR spectrum centred at a g value of approximately 1.93 (Fig. 3a), which can be ascribed to the emergence of Mo(V) species[52,53,54]. The unresolved hyperfine splitting and the asymmetric lineshape, which almost resemble a broad iso-tropic line, point to a Mo(V) centre with six oxygen atoms at close bond lengths where free movement or rotation is relatively unhindered[55]. Afterwards, the EPR tube containing Pd/CsPMA-H was vacuumized and purged with N_2 (denoted as Pd/CsPMA-H_2-N_2). This treatment resulted in an anisotropic EPR spectrum with a much narrower line-shape and resolution of the splitting that arises from the hyperfine interaction of the unpaired electron in Mo(V) with the ^{95}Mo and ^{97}Mo nuclei, both with a nuclear spin of $I = 5/2$ and a combined natural abundance of 25.5%. This spectral change implies a large extent of anisotropic distortion of the MoO_x polyhedra after reduction (Fig. 3a). The spectrum of the reduced sample was further fitted with g and A eigenframes, which are considered collinear, on the basis of previ-ous work and theoretical considerations[56–59]. Based on simulation results (Fig. 3b, Supplementary Fig. 22 and Supplementary Table 7), the spectrum consists of the signals of three Mo(V) components, with the dominant one containing an oxygen vacancy on the bridge site of two MoO_x polyhedra, signified as **F** (g = 1.954–1.955, $g_{\parallel}$ = 1.857, weight = 62%) (Supplementary Fig. 23)[60,61]. The remaining signals originate from pentacoordinated Mo(V) without molybdenyl oxygen (structure **C**) and the hexacoordinated Mo(V) centre (structure **A**)[60,61]. Although the results cannot give information on EPR-silent, deep reduced Mo(IV) species, the insights about Mo(V) already provide knowledge on the largely weakened Mo–O bonds and the tendency for oxygen deficiency around Mo centres under the reduced state that may facilitate interactions with oxygen or methane molecules.

When Pd/CsPMA-H was exposed to CH_4 and then analysed via EPR (Fig. 3a, pink trace), the spectrum exhibited a similar pattern to Pd/CsPMA-H_2-N_2 (light blue trace), which illustrates that the reduced Mo does not coordinate directly with methane molecules. However, when Pd/CsPMA-H was exposed to air, the EPR signals disappeared rapidly (purple and orange traces). Fully consistent with the EPR data, in situ Raman experiments reveal that Mo–O_b–Mo and Mo–O_c–Mo are sub-stantially weakened by H_2 reduction, which is recovered after treatment with O_2 (Supplementary Fig. 24). On the basis of these results, we posit that the MoO_x sites with oxygen vacancies first activate O_2, creating active surface oxygen to then enable C–H activation by abstracting a hydrogen atom from methane.

To confirm that O_2 fills the as-formed oxygen vacancies, we designed isotope labelling experiments using $^{18}O_2$ and $H_2{}^{18}O$ for methane oxidation reactions (Fig. 3c). For the standard methanol solution (leftmost trace) and methanol produced from methane in the presence of $H_2{}^{16}O$ and $^{16}O_2$ (left-middle trace), two major peaks appear, at $[CH_3{}^{16}O]^+$ (mass-to-charge ratio (m/z) = 31) and $[CH^{16}O]^+$ (m/z = 29). When $^{18}O_2$ was used as the oxidant (right-middle trace), the two peaks shifted to m/z = 33 and m/z = 31, respectively, confirming that ^{18}O-labelled methanol ($CH_3{}^{18}OH$) is the predominant product. In the case where $H_2{}^{18}O$ was used to replace normal water as the solvent (right-most trace), no increase in the m/z value was observed, indicating that oxygen in water is not the source of oxygen for methanol formation. These results demonstrate that the oxygen in the methanol product comes from O_2, consistent with our proposed mechanism in which O_2 fills the oxygen vacancies and is then incorporated into methane to form methanol, accompanied by O–O dissociation.

Theoretical insights into the formation of methanol over Pd/CsPMA-H

Density functional theory (DFT) calculations were performed to further verify the potential mechanisms for methane activation and methanol formation over the Pd/CsPMA-H catalyst (Fig. 4 and Supplementary Fig. 25). Considering that the donation of the electron by Cs is also simi-larly provided by spilled hydrogen and Cs^+ does not directly participate in methane activation, the Pd/PMA cluster (**I**) was constructed as the computational model. For the creation of active sites, calculations show that H_2 activation (**II**) occurs heterolytically over the Pd single-atom site with a relatively low barrier of 0.40 eV in terms of the enthalpy (H), resulting in a species with a hydroxyl group and PdH (intermediate **III**). Subsequently, hydrogen spillover to two neighbouring oxygen sites is thermodynamically favourable (intermediate **IV**), followed by H_2O generation with a slightly higher barrier of 0.50 eV (intermediate **V**). On

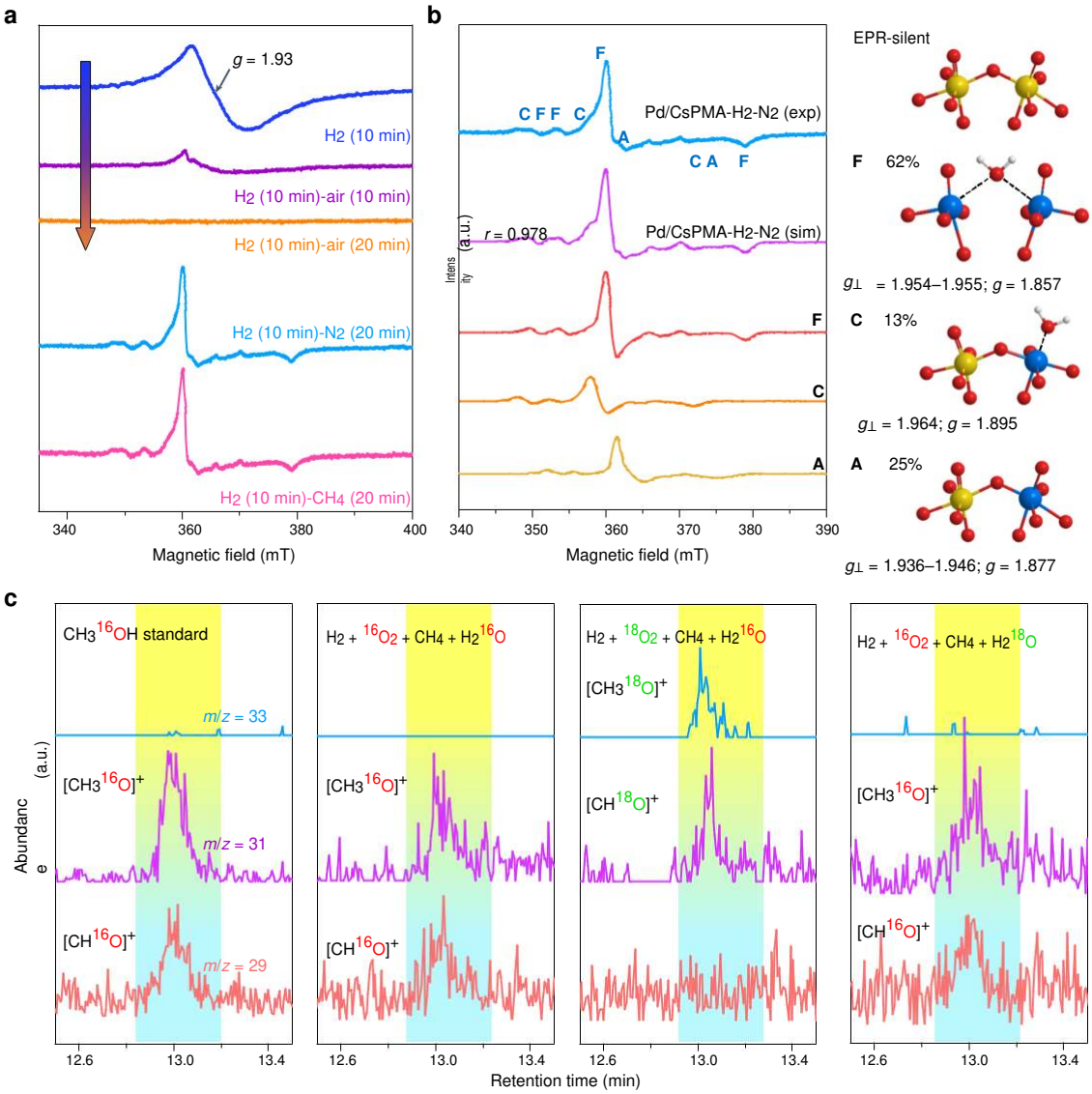

Fig. 3 | Experimental insights into the methane oxidation mechanism over Pd/CsPMA-H. a, Pseudo in situ EPR spectra of the Pd/CsPMA catalyst after treatment with different gases for different times. The label 'air' indicates the removal of the cover of the EPR tube and allowing the air to diffuse towards the catalyst at the bottom of the EPR tube. **b**, Experimental (exp) and simulated (sim) EPR spectra of the Pd/CsPMA-H solid under N_2. The simulated spectra of the individual species are presented (left) with the corresponding *g* values, weights and local structures (right). Atom colour code: O, red; H, light grey; Mo(VI), yellow; Mo(V), blue. *r*, Pearson correlation coefficient. **c**, Gas chromatography– mass spectrometry chromatograms of the extracted fragment ions (*m*/*z* = 29, 31 and 33) of methanol in a standard solution or produced from the partial oxidation of methane over Pd/CsPMA-H with $^{16}O_2 + H_2{}^{16}O$, $^{18}O_2 + H_2{}^{16}O$ and $^{16}O_2 + H_2{}^{18}O$, respectively. The highlighted region of 12.9–13.2 min indicates the retention time of methanol.

formation, the H_2O species remains adsorbed, bridging two Mo sites, O_2 has become highly activated and could be reactive to methane. In and subsequently desorbs to the gas phase to create an oxygen vacancy accordance with this expectation, C–H bond activation on the adsorbed that is energetically uphill by 0.81 eV in *H* but 0.27 eV in terms of the Gibbs free energy (*G*) (intermediate **VI**). Bader charge extrapolation was carried out, with the results showing that the oxidation state of one of the Mo atoms adjacent to the bridge oxygen vacancy is EPR-active Mo(V), corresponding well with the EPR results (Supplementary Fig. 26). The lattice oxygen vacancy in the bridging oxygen site is unreactive towards methane but can readily adsorb O_2 from the gas phase, with an adsorption energy of −0.14 eV and 0.46 eV in terms of *H* and *G*, respectively (intermediate **VII**). In this adsorbed state, one oxygen atom from O_2 is situated in the lattice oxygen position, while the second oxygen extends away from the surface and does not chemically bond with it. The O–O bond length of the adsorbed species is also elongated from the DFT gas-phase length of 1.23 Å to 1.32 Å, suggesting that the O_2 occurs with a barrier of 0.61 eV to form an O_2H species and a methyl radical (intermediates **VIII** and **IX**). Subsequently, the methyl radical can be captured by the same O_2H species via a rebound adsorption mechanism with a negligible barrier to form methanol, simultaneously cleaving the O–O bond and regenerating the lattice oxygen site (intermediate **X**). Considering the degree of reduction observed experimentally, we also mapped the reaction pathway with a POM containing eight adsorbed hydrogen species being reduced by eight electrons (Supplementary Figs. 27–29 and Supplementary Note 1). The profile shows that a reduced state of the POM favours H_2O desorption and O_2 adsorption, that is, the formation of active sites, without noticeably elevating the C–H activation barrier, which explains the surge in the methane activation performance over a reduced POM.

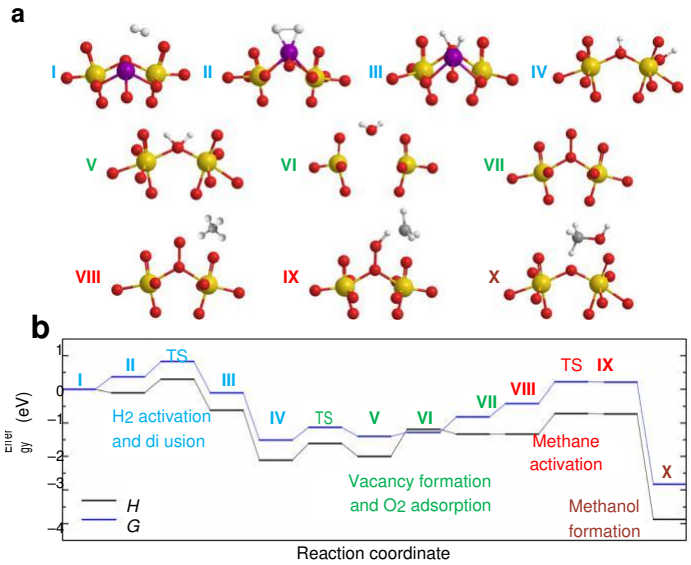

Fig. 4 | Proposed mechanism for methane activation and methanol formation from DFT calculations. a,**b**, The reaction intermediates (**a**) and the reaction profiles for both the enthalpy (*H*) and the Gibbs free energy (*G*) (**b**). The reaction proceeds initially via H_2 activation and diffusion (intermediates **I**–**IV**), followed by vacancy formation and O_2 adsorption (intermediates **V**–**VII**), then methane activation (intermediates **VIII and IX**) and methanol formation (intermediate **X**). Atom colour code: Mo, yellow; Pd, purple; O, red; C, dark grey; H, light grey. TS, transition state.

In this mechanism, methane activation is enabled by the formation of activated O_2 species that result from hydrogen spillover and vacancy formation. The rate-limiting step is C–H activation, in agreement with the experimentally observed first-order kinetics for methane. We also find that this mechanism agrees with the volcano-type curve for the H_2/O_2 ratio, as a balance must be struck to ensure the survival of the activated O_2 species (intermediate **VI**). An overabundance of gaseous O_2 will react with hydroxyl groups and prevent vacancy formation, whereas an overabundance of H_2 will probably react with the adsorbed O_2 before it can activate the methane. The mechanism was calculated on oxygen/vacancy sites that are non-adjacent to Pd, indicating that the presence of Pd was not required for methanol formation beyond the initial H_2 activation step, in accordance with the poisoning studies. Alternative mechanisms were also considered but were found to be unfavourable or inconsistent with experimental observations (Sup-plementary Figs. 30–32 and Supplementary Note 2).

Conclusions

In summary, we report a Pd-immobilized CsPMA catalyst with H_2-reduced Mo sites for the aerobic oxidation of methane to methanol, with the entire process operated at ambient temperature. Under the optimum conditions the catalyst achieved a methanol productivity of 29.3 mmol g_{Pd}^{-1} h^{-1} or 67.4 μmol g_{cat}^{-1} h^{-1} with nearly 100% selectiv-ity at room temperature. Partially reduced Mo on PMA bears oxygen vacancies at the bridge sites, which readily activate O_2 via a refilling mechanism, creating active oxygen for hydrogen-atom abstraction from methane. Pd enables H_2 activation and PMA reduction, but does not participate in methane conversion. These findings provide a system for the selective synthesis of methanol from methane using O_2 as the oxidant and H_2 as the activating agent at ambient temperature, without the use of an external energy source (for example, light or electricity). From a mechanistic perspective, the Mo centre in its partially reduced state is found to be critical for an oxidation reaction to generate active oxygen species from O_2, which extends our understanding of typical catalytic oxidation processes.

Methods

Sample preparation

Phosphomolybdic acid hydrate (PMA hydrate; $H_3PMo_{12}O_{40}{\cdot}xH_2O$), phosphotungstic acid hydrate (PTA hydrate; $H_3PW_{12}O_{40}{\cdot}xH_2O$), palladium(II) nitrate hydrate ($Pd(NO_3)_2{\cdot}xH_2O$, ~40% Pd basis), rhodium(III) trinitrate hydrate ($Rh(NO_3)_3{\cdot}xH_2O$, ~36% Rh basis), H_2O_2 (35%) and dimethyl sulfoxide (DMSO; anhydrous, ≥99.9%) were obtained from Sigma-Aldrich. Platinum(IV) nitrate solution (15% Pt basis) was obtained from Alfa Aesar. Deuterium oxide (D_2O; D, 99.9%) was obtained from Cambridge Isotope Laboratories. All the chemicals were used without further treatment. A co-precipitation method was adopted for the synthesis of different samples. Taking Pd/CsPMA as an example, PMA hydrate (1.5 g) was dissolved in ultrapure water (30 ml) acidified with two drops of concentrated HNO_3 (65–68%) to obtain the heteropoly acid solution. The cation stock solution was prepared by adding $CsNO_3$ (390 mg) and $Pd(NO_3)_2{\cdot}xH_2O$ (28 mg) to ultrapure water (30 ml) with two drops of concentrated HNO_3. Afterwards, the cation solution containing Cs^+ and Pd^{2+} was added dropwise into the ice-bathed heteropoly acid solution (at 0 °C) at a rate of around 1 ml min^{-1} under rigorous stirring, during which the yellow precipitate appeared gradually. Stirring of the mixed suspension was continued for another 5 h at 0 °C, followed by centrifugation to separate the solid. The solid was washed further with ultrapure water three times, dried using a freeze-dryer, and carefully ground for use. To obtain the POM without Pd, the cation solution contained only Cs^+ for the precipitation of $[PMo_{12}O_{40}]^{3-}$. As for Pd/CsPTA, PTA hydrate (2.16 g) was used as the POM precursor instead, while the amount of $Pd(NO_3)_2$ hydrate was adjusted to 8.6 mg.

Characterization

A field-emission scanning electron microscope (Hitachi, SU8010) and a transmission electron microscope (Thermo Fisher Scientific, Talos F200S) were employed to observe the morphology and crys-tallinity of the catalyst. HAADF and iDPC imaging were carried out using an aberration-corrected scanning transmission electron micro-scope (AC-STEM; Thermo Fisher Scientific, Themis Z) to observe the atomic arrangement in the crystalline catalyst. An X-ray diffractometer (Rigaku, MiniFlex 600) with Cu Kα1 radiation was used to determine the phase structure. The surface area of the sample was determined using the Brunauer–Emmett–Teller method. Raman spectroscopy (Horiba, LabRAM HR Evolution) was performed with an excitation laser wavelength of 532 nm to reflect the structure of POM.

XPS (Thermo Fisher Scientific, ESCALAB250Xi) was adopted to characterize the oxidation states of the elements. UV-visible absorption spectroscopy (Hitachi, UH5300) was used to probe the chemical state of Mo of the catalyst in water. EPR (Bruker, model A300) spectra were acquired at the X band for the detection of radicals and excited species in suspensions and paramagnetic metal species in powder samples (that is, Mo(V)). For pseudo in situ EPR, the quartz tube containing the sample was filled with a specific gas and sealed in a glove box, followed by spectral acquisition. To replace the atmosphere, the EPR tube was vacuumized and purged with the aim gas three times. The simulation of EPR spectra was carried out using the EasySpin toolbox running in Matlab R2020b (ref. 62).

DRIFTS experiments were carried out using an Fourier transform infrared spectrometer (Thermo Fisher Scientific, Nicolet iS50) with a mercury cadmium telluride detector working at liquid nitrogen temperature. The catalysts were loaded and smoothed in an in situ DRIFTS cell with a zinc selenide window. All spectra were recorded in terms of their absorbance at a resolution of 4 cm^{-1} with 64 scans at room temperature and atmospheric pressure. The background was initially obtained under a flow of N_2 at 40 ml min^{-1} until the spectrum become steady. For in situ NO-DRIFTS experiments, 1% NO/Ar was subsequently introduced at a rate of 40 ml min^{-1} for 10 min, while DRIFT spectra were collected in the meantime. For H_2-DRIFTS experiments, purified H_2 was purged at a rate of 40 ml min^{-1} for 10 min, followed by N_2 sweeping for another 10 min before the stabilized spectra were recorded.

Performance evaluation

The performance of partial methane oxidation was tested using a stainless-steel autoclave equipped with a 10 ml glass vial liner. For a typical procedure, 10 mg of the catalyst was dispersed in D_2O (2.0 ml) in the glass vial. Then the catalyst suspension was exposed to a mixture of methane and O_2 (where the partial pressures are 10 bar and 1 bar, respectively). The dispersed catalyst was first stirred at 800 revolu-tions per minute (r.p.m.) under H_2 (4 bar) for 15 min to reach a sufficient hydrogen-spillover state. For running the methane oxidation reaction with a H_2 cofeed, the autoclave was pressurized with the reactant gases (H_2, O_2 and methane) balanced with inert gas (N_2 and Ar). Then the liquid mixture was stirred at 800 r.p.m. at a specific temperature for 30 min. When H_2O_2 was used as the oxidant, the solvent used was ultrapure water (2.0 ml) (with a specific amount of H_2O_2). The autoclave was then filled with methane (10 bar) without H_2 and O_2. After the reaction, the gases in the autoclave were collected using a gas sampling bag and analysed using a gas chromatograph (Agilent, 7890B) with Porapak-Q and molecular sieve 5A columns and a thermal conductivity detector using helium as the carrier gas. The oxygenated products in the liquid solution were detected and quantified using ^{1}H NMR spectroscopy (400 MHz, Bruker). For D_2O-based experiments, the sample (1.0 ml) was mixed with D_2O solution (50 µl) containing DMSO (0.50 µmol), which acts as the internal standard. For samples with H_2O as the solvent, the sample (1.0 ml), D_2O (0.15 ml) and the same DMSO solution (50 µl) were mixed thoroughly, placed in an NMR tube and then detected under water-suppression mode.

For stability testing, Pd/CsPMA (10 mg) was dispersed in D_2O (2.0 ml) and first treated with H_2 (1 bar) in the autoclave for 18 min, after which the catalyst was exposed to a mixture of H_2 (1 bar), O_2 (0.4 bar), N_2 (28.6 bar) and CH_4 (20 bar) and then stirred for 1–8 h for the reaction.

For the recycling tests, Pd/CsPMA (10 mg) was dispersed in D_2O (2.0 ml) and exposed to the reaction atmosphere (H_2 (2 bar), O_2 (0.3 bar) and CH_4 (10 bar) balanced with N_2 (25.7 bar)) at room temperature for 30 min. Then a 200 µl aliquot of the reaction mixture was extracted, which was mixed with D_2O (400 µl) containing DMSO (0.25 µmol) for the ^{1}H NMR test. The remaining suspension with the reduced cata-lyst was treated with a mixture of O_2 (1 bar) and N_2 (9 bar) for 30 min, followed by the addition of $CsNO_3$ (5 mg) to fully precipitate the dis-solved PMA. The solid was centrifuged to separate it from the liquid. Thereafter, a suitable amount of D_2O was added to maintain the same concentration of Pd/CsPMA in the solution as that of the first run. The mixture was then used for the methane oxidation reaction under the same reaction conditions, followed by the same recycling procedure.

For the ^{18}O isotope labelling experiments, Pd/CsPMA (10 mg) was dispersed in H_2O (2.0 ml) and first pretreated with H_2 (1 bar) for 18 min, followed by purging with N_2 three times. Then, H_2 (1 bar), $^{16}O_2$ or $^{18}O_2$ (0.4 bar), N_2 (18.6 bar) and CH_4 (30 bar) were introduced and reacted for 1 h. Afterwards, the reaction mixture was purged further with N_2 three times, after which $^{16}O_2$ or $^{18}O_2$ (0.2 bar) balanced with N_2 was introduced and stirred for 30 min to reoxidize the catalyst, so that the catalyst can be separated from the solution. The supernatant was then analysed using off-line gas chromatography–mass spectrometry (Agilent 7890A/5975C GC/MSD system). An HP-INNOWax column was used for measuring the water-containing sample.

DFT calculations

DFT calculations were performed with using the Vienna ab initio simulation package[63,64]. The Perdew–Burke–Ernzerhof functional form of the generalized-gradient approximation for electron exchange and correlation energies was used[65]. Spin polarization was considered for all calculations. The projector-augmented wave method was used to describe the electron–core interaction with a kinetic energy cutoff of 450 eV (refs. 63,66). A cubic cell with cell lengths of 20 Å was used to ensure a sufficient distance between the images. Geometry optimiza-tions were performed to a force convergence of 0.02 eV Å^{-1}. Transition states were obtained using the nudged elastic band[67] method using a force convergence criterion of 0.05 eV Å^{-1}.

Data availability

All data are available from the authors upon reasonable request. Source data are provided with this paper.

References

1.\ Sushkevich, V. L., Palagin, D., Ranocchiari, M. & Bokhoven, J. A. V. Selective anaerobic oxidation of methane enables direct synthesis of methanol. *Science* **356**, 523–527 (2017).

2.\ Shan, J., Li, M., Allard, L. F., Lee, S. & Flytzani-Stephanopoulos, M. Mild oxidation of methane to methanol or acetic acid on supported isolated rhodium catalysts. *Nature* **551**, 605–608 (2017).

3.\ Schwach, P., Pan, X. & Bao, X. Direct conversion of methane to value-added chemicals over heterogeneous catalysts: challenges and prospects. *Chem. Rev.* **117**, 8497–8520 (2017).

4.\ Wang, V. C. et al. Alkane oxidation: methane monooxygenases, related enzymes, and their biomimetics. *Chem. Rev.* **117**, 8574– 8621 (2017).

5.\ Meng, X. et al. Direct methane conversion under mild condition by thermo-, electro-, or photocatalysis. *Chem* **5**, 2296–2325 (2019).

6.\ Sher Shah, M. S. A. et al. Catalytic oxidation of methane to oxygenated products: recent advancements and prospects for electrocatalytic and photocatalytic conversion at low temperatures. *Adv. Sci.* **7**, 2001946 (2020).

7.\ *Resources to Reserves 2013* (IEA, 2013).

8.\ Koo, C. W. & Rosenzweig, A. C. Biochemistry of aerobic biological methane oxidation. *Chem. Soc. Rev.* **50**, 3424–3436 (2021).

9.\ Hammond, C. et al. Direct catalytic conversion of methane to methanol in an aqueous medium by using copper-promoted Fe-ZSM-5. *Angew. Chem. Int. Ed.* **51**, 5129–5133 (2012).

10.\ Qi, G. et al. Au-ZSM-5 catalyses the selective oxidation of CH_4 to CH_3OH and CH_3COOH using O_2. *Nat. Catal.* **5**, 45–54 (2022).

11.\ Baek, J. et al. Bioinspired metal–organic framework catalysts for selective methane oxidation to methanol. *J. Am. Chem. Soc.* **140**, 18208–18216 (2018).

12.\ Ikuno, T. et al. Methane oxidation to methanol catalyzed by Cu-oxo clusters stabilized in NU-1000 metal–organic framework. *J. Am. Chem. Soc.* **139**, 10294–10301 (2017).

13.\ Zheng, J. et al. Selective methane oxidation to methanol on Cu-oxo dimers stabilized by zirconia nodes of an NU-1000 metal–organic framework. *J. Am. Chem. Soc.* **141**, 9292–9304 (2019).

14.\ Osadchii, D. Y. et al. Isolated Fe sites in metal organic frameworks catalyze the direct conversion of methane to methanol. *ACS Catal.* **8**, 5542–5548 (2018).

15.\ Huang, W. et al. Low-temperature transformation of methane to methanol on Pd_1O_4 single sites anchored on the internal surface of microporous silicate. *Angew. Chem. Int. Ed.* **55**, 13441–13445 (2016).

16.\ Kwon, Y., Kim, T. Y., Kwon, G., Yi, J. & Lee, H. Selective activation of methane on single-atom catalyst of rhodium dispersed on zirconia for direct conversion. *J. Am. Chem. Soc.* **139**, 17694– 17699 (2017).

17.\ Cui, X. et al. Room-temperature methane conversion by graphene-confined single iron atoms. *Chem* **4**, 1902–1910 (2018).

18.\ Shen, Q. et al. Single chromium atoms supported on titanium dioxide nanoparticles for synergic catalytic methane conversion under mild conditions. *Angew. Chem. Int. Ed.* **59**, 1216–1219 (2020).

19.\ Bai, S. et al. High-efficiency direct methane conversion to oxygenates on a cerium dioxide nanowires supported rhodium single-atom catalyst. *Nat. Commun.* **11**, 954 (2020).

20.\ Tang, X. et al. Direct oxidation of methane to oxygenates on supported single Cu atom catalyst. *Appl. Catal. B* **285**, 119827 (2021).

21.\ Ab Rahim, M. H. et al. Oxidation of methane to methanol with hydrogen peroxide using supported gold–palladium alloy nanoparticles. *Angew. Chem. Int. Ed.* **52**, 1280–1284 (2013).

22.\ Agarwal, N. et al. Aqueous Au–Pd colloids catalyze selective CH_4 oxidation to CH_3OH with O_2 under mild conditions. *Science* **358**, 223–227 (2017).

23.\ Chen, J. et al. Oxidation of methane to methanol over Pd@Pt nanoparticles under mild conditions in water. *Catal. Sci. Technol.* **11**, 3493–3500 (2021).

24.\ He, Y. et al. Low-temperature direct conversion of methane to methanol over carbon materials supported Pd–Au nanoparticles. *Catal. Today* **339**, 48–53 (2020).

25.\ Bai, S., Xu, Y., Wang, P., Shao, Q. & Huang, X. Activating and converting CH_4 to CH_3OH via the $CuPdO_2$/CuO nanointerface. *ACS Catal.* **9**, 6938–6944 (2019).

26.\ Wu, B. et al. Cu single-atoms embedded in porous carbon nitride for selective oxidation of methane to oxygenates. *Chem. Commun.* **56**, 14677–14680 (2020).

27.\ Xie, J. et al. Highly selective oxidation of methane to methanol at ambient conditions by titanium dioxide-supported iron species. *Nat. Catal.* **1**, 889–896 (2018).

28.\ McVicker, R. et al. Low temperature selective oxidation of methane using gold–palladium colloids. *Catal. Today* **342**, 32–38 (2020).

29.\ Jin, Z. et al. Hydrophobic zeolite modification for in situ peroxide formation in methane oxidation to methanol. *Science* **367**, 193–197 (2020).

30.\ Kang, J. & Park, E. D. Selective oxidation of methane over Fe-zeolites by in situ generated H_2O_2. *Catalysts* **10**, 299 (2020).

31.\ Kang, J., Puthiaraj, P., Ahn, W.-s. & Park, E. D. Direct synthesis of oxygenates via partial oxidation of methane in the presence of O_2 and H_2 over a combination of Fe-ZSM-5 and Pd supported on an acid-functionalized porous polymer. *Appl. Catal. A* **602**, 117711 (2020).

32.\ Luo, L. et al. Synergy of Pd atoms and oxygen vacancies on In_2O_3 for methane conversion under visible light. *Nat. Commun.* **13**, 2930 (2022).

33.\ An, B. et al. Direct photo-oxidation of methane to methanol over a mono-iron hydroxyl site. *Nat. Mater.* **21**, 932–938 (2022).

34.\ Fan, Y. et al. Selective photocatalytic oxidation of methane by quantum-sized bismuth vanadate. *Nat. Sustain.* **4**, 509–515 (2021).

35.\ Srivastava, R. K., Sarangi, P. K., Bhatia, L., Singh, A. K. & Shadangi, K. P. Conversion of methane to methanol: technologies and future challenges. *Biomass. Convers. Biorefin.* **12**, 1851–1875 (2021).

36.\ Lopez, X., Carbo, J. J., Bo, C. & Poblet, J. M. Structure, properties and reactivity of polyoxometalates: a theoretical perspective. *Chem. Soc. Rev.* **41**, 7537–7571 (2012).

37.\ Wang, S.-S. & Yang, G.-Y. Recent advances in polyoxometalate-catalyzed reactions. *Chem. Rev.* **115**, 4893–4962 (2015).

38.\ Zhang, B. et al. Stabilizing a platinum$_1$ single-atom catalyst on supported phosphomolybdic acid without compromising hydrogenation activity. *Angew. Chem. Int. Ed.* **55**, 8319–8323 (2016).

39.\ Zhang, B. et al. Atomically dispersed Pt_1-polyoxometalate catalysts: how does metal–support interaction affect stability and hydrogenation activity? *J. Am. Chem. Soc.* **141**, 8185–8197 (2019).

40.\ Hülsey, M. J., Fung, V., Hou, X., Wu, J. & Yan, N. Hydrogen spillover and its relation to hydrogenation: observations on structurally defined single-atom sites. *Angew. Chem. Int. Ed.* **61**, e202208237 (2022).

41.\ Hülsey, M. J. et al. Identifying key descriptors for the single-atom catalyzed CO oxidation. *CCS Chem.* **4**, 3296–3308 (2022).

42.\ Geng, Y. & Li, H. Hydrogen spillover-enhanced heterogeneously catalyzed hydrodeoxygenation for biomass upgrading. *ChemSusChem* **15**, e202102495 (2022).

43.\ Xiong, M., Gao, Z. & Qin, Y. Spillover in heterogeneous catalysis: new insights and opportunities. *ACS Catal.* **11**, 3159–3172 (2021).

44.\ Xi, Q. et al. In-situ fabrication of MoO_3 nanobelts decorated with MoO_2 nanoparticles and their enhanced photocatalytic performance. *Appl. Surf. Sci.* **480**, 427–437 (2019).

45.\ Dieterle, M., Weinberg, G. & Mestl, G. Raman spectroscopy of molybdenum oxides. *Phys. Chem. Chem. Phys.* **4**, 812–821 (2002).

46.\ Ravi, M. et al. Misconceptions and challenges in methane-to-methanol over transition-metal-exchanged zeolites. *Nat. Catal.* **2**, 485–494 (2019).

47.\ Richards, T. et al. A residue-free approach to water disinfection using catalytic in situ generation of reactive oxygen species. *Nat. Catal.* **4**, 575–585 (2021).

48.\ Fontmorin, J. M., Burgos Castillo, R. C., Tang, W. Z. & Sillanpaa, M. Stability of 5,5-dimethyl-1-pyrroline-*N*-oxide as a spin-trap for quantification of hydroxyl radicals in processes based on Fenton reaction. *Water Res.* **99**, 24–32 (2016).

49.\ Conte, M. et al. Insights into the reaction mechanism of cyclohexane oxidation catalysed by molybdenum blue nanorings. *Catal. Lett.* **146**, 126–135 (2016).

50.\ Liu, X. et al. Molybdenum blue nano-rings: an effective catalyst for the partial oxidation of cyclohexane. *Catal. Sci. Technol.* **5**, 217–227 (2015).

51.\ Cozar, O., Magdas, D. A. & Ardelean, I. EPR study of molybdenum-lead-phosphate glasses. *J. Non-Cryst. Solids* **354**, 1032–1035 (2008).

52.\ Almidani, A. H. et al. The reaction of $HV(CO)_4$dppe with MoO_3: a well-defined model of hydrogen spillover. *Catal. Sci. Technol.* **11**, 7540–7544 (2021).

53.\ Timmiati, S. N., Jalil, A. A., Triwahyono, S., Setiabudi, H. D. & Annuar, N. H. R. Formation of acidic Brönsted $(MoO_x)^-(H_y)^+$ evidenced by XRD and 2,6-lutidine FTIR spectroscopy for cumene cracking. *Appl. Catal. A* **459**, 8–16 (2013).

54.\ Triwahyono, S., Jalil, A. A., Ruslan, N. N., Setiabudi, H. D. & Kamarudin, N. H. N. C_5–C_7 linear alkane hydroisomerization over MoO_3–ZrO_2 and Pt/MoO_3–ZrO_2 catalysts. *J. Catal.* **303**, 50–59 (2013).

55.\ Spencer, J., Folli, A., Richards, E. & Murphy, D. M. in *Electron Paramagnetic Resonance*, Vol. 26 (eds Chechik, V. & Murphy, D. M.) 130–170 (Royal Society of Chemistry, 2018).

56.\ Selvaraj, U. & Rao, K. J. ESR and optical studies of Mo^{5+} and W^{5+} ions in phosphomolybdate and phosphotungstate glasses. *Chem. Phys.* **123**, 141–150 (1988).

57.\ Kivelson, D. & Lee, S. K. ESR studies and the electronic structure of vanadyl ion complexes. *J. Chem. Phys.* **41**, 1896–1903 (2004).

58.\ Abragam, A., Pryce, M. H. L. & Simon, F. E. Theory of the nuclear hyperfine structure of paramagnetic resonance spectra in crystals. *Proc. R. Soc. Lond. A Math. Phys. Sci.* **205**, 135–153 (1951).

59.\ Abragam, A., Pryce, M. H. L. & Bleaney, B. The theory of the nuclear hyperfine structure of paramagnetic resonance spectra in the copper Tutton salts. *Proc. R. Soc. Lond. A Math. Phys. Sci.* **206**, 164–172 (1951).

60.\ Łabanowska, M. EPR monitoring of redox processes in transition metal oxide catalysts. *ChemPhysChem* **2**, 712–731 (2001).

61.\ Łabanowska, M. Paramagnetic defects in MoO_3—revisited. *Phys. Chem. Chem. Phys.* **1**, 5385–5392 (1999).

62.\ Stoll, S. & Schweiger, A. EasySpin, a comprehensive software package for spectral simulation and analysis in EPR. *J. Magn. Reson.* **178**, 42–55 (2006).

63.\ Kresse, G., & Furthmüller, J. Efficiency of ab-initio total energy calculations for metals and semiconductors using a plane-wave basis set. *Comput. Mater. Sci.* **6**, 15–50 (1996).
64.\ Kresse, G. & Furthmüller, J. Efficient iterative schemes for ab initio total-energy calculations using a plane-wave basis set. *Phys. Rev. B* **54**, 11169–11186 (1996).
65.\ Perdew, J. P., Burke, K. & Ernzerhof, M. Generalized gradient approximation made simple. *Phys. Rev. Lett.* **77**, 3865–3868 (1996).
66.\ Blöchl, P. E. Projector augmented-wave method. *Phys. Rev. B* **50**, 17953–17979 (1994).
67.\ Henkelman, G., Uberuaga, B. P. & Jónsson, H. A. Climbing image nudged elastic band method for finding saddle points and minimum energy paths. *J. Chem. Phys.* **113**, 9901–9904 (2000).

Acknowledgements

We thank the National Natural Science Foundation of China (92061109) for supporting the project. N.Y. and Q.H. sincerely acknowledge the support of the National Research Foundation (NRF) Singapore, under its NRF Investigatorship (NRF-NRFI07–2021–0006) and NRF Fellowship (NRF-NRFF11-2019-0002), respectively. R.J.L. and G.J.H. gratefully acknowledge Cardiff University and the Max Planck Centre for Fundamental Heterogeneous Catalysis (FUNCAT) for financial support. Z.Y. acknowledges support from the National Natural Science Foundation of China (52222102, 22272024 and 51871058) and the Eyas Program of Fujian Province. DFT simulations were conducted at the Center for Nanophase Materials Sciences (CNMS), which is a US Department of Energy, Office of Science User Facility at Oak Ridge National Laboratory.

Author contributions

N.Y. conceived and supervised the project. Q.H. and G.J.H. co-supervised the project. S.W. conducted most experiments including synthesis, characterization and testing, as well as data analysis. V.F. carried out DFT calculations and wrote the related section. M.J.H. and J.C. carried out the catalyst synthesis and characterization. X.L. and Z.Y. conducted TEM analysis. A.F. and R.J.L. contributed to data analysis of the EPR spectra and H_2O_2 detection. S.W., Q.H. and N.Y. wrote the paper. G.J.H., A.F. and R.J.L. revised the paper. All authors discussed the paper.

Competing interests

The authors declare no competing interests.

Additional information

Supplementary information The online version contains supplementary material available at https://doi.org/10.1038/s41929-023-01011-5.

Correspondence and requests for materials should be addressed to Graham J. Hutchings, Qian He or Ning Yan.